Flow in a rotating curved circular pipe

Jinsuo Zhang,[1,2,*] Ning Li,[1] and Benzhao Zhang[2]
[1]*Los Alamos National Laboratory, Los Alamos, New Mexico 87545*
[2]*Mechanics Department, Zhejiang University, Hangzhou 310027, People's Republic of China*
(Received 30 July 2002; published 12 May 2003)

The flow in a rotating curved pipe with circular cross section is investigated theoretically and numerically. A perturbation solution up to the second order is obtained. A numerical procedure is used to solve the full governing equations and the simplified governing equations in the small curvature limit. Comparisons are made between the numerical and perturbation results, elucidating the lost information due to simplification and the valid range of the perturbation solution. The flow characteristics, including the secondary flow, the axial flow, and the friction factor ratio, are examined in detail.

DOI: 10.1103/PhysRevE.67.056303 PACS number(s): 47.60.+i, 83.50.Ha

I. INTRODUCTION

Fluid flow through curved pipes is very common. It can be found in nature, e.g., in blood vessels, particularly the aorta and the trachea, or engineering applications. With the popularity of the rotary machinery in industry, the characteristics of the flow in the control pipe system, the transport pipe system, and the coolant pipe system are among the main factors to improve the efficiencies of the rotary machinery. Consequently, understanding flows in rotating pipes has become one of the urgent problems in engineering and one of the challenging research fields in fluid mechanics. Analyzing these types of flows requires an interesting nonlinear model. Complex secondary flows exist and flow bifurcation may occur under some conditions.

Because of their wide spectrum of applications and richness in physical phenomena, flows in rotating curved pipes have been studied by many researchers since the first work of Ludwieg [1] who analyzed the flow in a rotating toroidally curved square duct based on the momentum integral method. Miyazaki studied the characteristics of the flow and heat transfer in the boundary layer of rotating toroidally curved circular pipe [2] and rectangular duct [3] using finite-difference method and predicted an increase of the friction factor with increasing rotation. These analyses were for the corotating cases, i.e., the rotating angular velocity and the axial flow velocity are in the same direction.

Ito and Motai [4] first studied the fluid flow in both corotating and counter-rotating (the rotating velocity and the axial flow velocity are in the opposite directions) curved ducts and predicted a reduction in strength and a reversal of the direction of the secondary flow for small curvatures and the Dean numbers. Menon [5] confirmed the reversal of the secondary flow even for the high Dean numbers. Ito *et al.* [6] studied the friction factor in a rotating toroidally curved pipe numerically and experimentally for the cases of the constant Dean number. Ishigaki [7] examined the flow characteristics and friction factor numerically for both counter-rotating and corotating curved pipes with small curvatures and a circular cross section. He introduced a new parameter F that represents the ratio of the Coriolis force to the centrifugal force and studied the flow transitions with the varying F for two Dean numbers. Wang and Cheng [8] studied the flow structure in a rotating toroidal square duct when the wall is heated or cooled. Yamamoto *et al.* [9], employing the spectral method, examined the flow structure and the flow rate for the flow in a rotating curved square duct. Zhang *et al.* [10] studied the flow structure and friction factor in a rotating rectangular duct for a wide range of rotation speeds and found more complex cell structures. Zhang *et al.* [11], employing the perturbation method, studied the flow in a toroidal annular pipe. Their work focused on the effect of the inner wall of the pipe and revealed an eight-cell structure of the secondary flow when F is around -1.

Bifurcation studies on the flow in rotating curved circular pipes were carried out by Daskopoulos and Lenhoff [12]. Selmi *et al.* [13] and Selmi and Nandakumar [14] also worked on the bifurcation of the flow in a rotating curved square duct. Wang and Cheng examined the flow instability in rotating rectangular duct experimentally for the counter-rotating case [15].

In practical applications, large curvatures are often encountered. But the existing studies on curved rotating pipe are almost all confined to small curvatures, based on the simplified governing equations, such as Daskopoulos and Lenhoff [12] and Ishigaki [7]. The simplification is expected to lose some flow information, especially the effects of the curvature, but there has been no study on the lost information and no study on the accuracy of the solutions obtained from the simplified equations. The present study is an attempt to fill these gaps. The full governing equations are solved numerically, and the simplified governing equations are solved numerically and analytically. Comparisons elucidate the accuracy of the simplified equations and the lost flow information through simplification.

This study is also partly motivated by Liu and Masliyah [16], who examined the effects of curvature on the flow in a stationary curved circular pipe and found some significant influences. In the present study, the curvature κ ($\kappa = d/R$, d is the diameter of the pipe and R is the radius of curvature) covers a range from 0.001 to 1.6. Results illustrate the effects

*Author to whom correspondence should be addressed. FAX: (505) 665-2659. Email address: izhang@cnls.lanl.gov

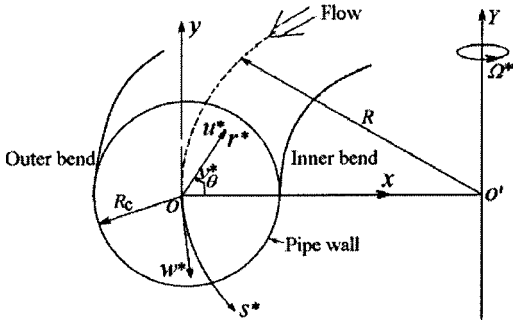

FIG. 1. The coordinate system and the rotating curved pipe.

of the curvature on the flow structure and the friction factor ratio.

Based on the above analysis, the present study serves two purposes: to elucidate the flow information lost through the use of the simplified equations, and to show the effects of the curvature on the flow. Comparisons are made between the results, which not only validate each other, but also elucidate the flow information lost because of the simplifications. We will examine the flow structure with varying curvature for the high and low Rossby numbers, and discuss the curvature effects in detail.

II. GOVERNING EQUATIONS

Figure 1 shows the rotating curved circular pipe and the coordinate system used in the paper. The coordinates are r^*, θ, s^*, where s^* is along the centerline of the pipe. The velocities in the directions of r^*, θ, s^* are denoted by u^*, v^*, w^*. The pipe rotates around the y axis with a constant angular velocity Ω^*. When $\Omega^*>0$, there is a corotation is meaning that the rotation is in the same direction with the axial flow. When $\Omega^*<0$ there is a counter-rotation. It is assumed that the flow is incompressible, steady, laminar, and fully developed. The following dimensionless parameters are introduced:

$$s=\frac{s^*}{d_h},\quad r=\frac{r^*}{d_h},\quad w=\frac{w^*}{w_m^*},\quad u=\frac{u^*d_h}{\upsilon},\quad v=\frac{v^*d_h}{\upsilon},$$

$$p=\frac{p^*d_h^2}{\rho\upsilon^2},\quad \Omega=\frac{\Omega^*d_h^2}{\upsilon},$$

where d_h is the hydraulic diameter ($d_h=2R_c=d$, R_c is the radius of the pipe). w_m^* is the dimensioned mean axial velocity, υ is the kinematic viscosity, and ρ is the fluid density. p and p^* are the dimensionless and dimensioned pseudopressures. The equations of the continuity and the momentum in the dimensionless forms are

$$\frac{\partial(Mru)}{\partial r}+\frac{\partial(Mv)}{\partial\theta}=0, \tag{1a}$$

$$u\frac{\partial u}{\partial r}+\frac{v}{r}\frac{\partial u}{\partial\theta}-\frac{v^2}{r}=-\frac{\partial p}{\partial r}-\mathrm{De}^2 w\cos\theta\left(\frac{w}{M}+2F\right)-\left(\frac{1}{r}\frac{\partial\xi_s}{\partial\theta}+\frac{\kappa\sin\theta}{M}\xi_s\right), \tag{1b}$$

$$u\frac{\partial v}{\partial r}+\frac{v}{r}\frac{\partial v}{\partial\theta}+\frac{uv}{r}=-\frac{1}{r}\frac{\partial p}{\partial\theta}+\mathrm{De}^2 w\sin\theta\left(\frac{w}{M}+2F\right)+\left(\frac{\partial\xi_s}{\partial r}-\frac{\kappa\cos\theta}{M}\xi_s\right), \tag{1c}$$

$$u\frac{\partial w}{\partial r}+\frac{v}{r}\frac{\partial w}{\partial\theta}=\frac{G}{M}+\frac{\kappa\cos\theta}{M}uw-\frac{\kappa\sin\theta}{M}vw+\frac{2}{\mathrm{Ro}}(u\cos\theta-v\sin\theta)+\left(\frac{1}{r}\frac{\partial\xi_r}{\partial\theta}-\frac{1}{r}\frac{\partial r\xi_\theta}{\partial r}\right), \tag{1d}$$

where $M=1-\kappa r\cos\theta$ and $G=-(\partial p/\partial s)/\mathrm{Re}$ is a constant. ξ_s, ξ_r, and ξ_θ are the vorticity components in (s,r,θ) and are defined as

$$\xi_s=\frac{1}{r}\frac{\partial rv}{\partial r}-\frac{1}{r}\frac{\partial u}{\partial\theta},\quad \xi_r=\frac{1}{r}\frac{\partial w}{\partial\theta}+\frac{\kappa\sin\theta}{M}w,$$

$$\xi_\theta=-\frac{\partial w}{\partial r}+\frac{\kappa\cos\theta}{M}w.$$

Four dimensionless parameters are defined as

$$\kappa=\frac{d_h}{R},\quad F=\frac{\Omega^*R}{w_m^*},\quad \mathrm{De}=\mathrm{Re}\sqrt{\kappa},\quad \mathrm{Ro}=\frac{w_m^*}{d_h\Omega^*},$$

where $\mathrm{Re}=w_m^*d_h/\upsilon$ is the Reynolds number, κ is the curvature, and De is the Dean number. F is a new parameter first used by Ishigaki [7] and represents the ratio of the Coriolis force to the centrifugal force. $F>0$ means corotation, and $F=0$ means the stationary. Ro is the Rossby number and represents the ratio of the inertial force to the Coriolis force. We easily find that Ro is not an independent parameter and can be written as $\mathrm{Ro}=1/(F\kappa)$.

An important characterization of the secondary flow is the stream function. To satisfy continuity equation (1a), the stream function ψ is introduced as

$$\frac{1}{r}\frac{\partial\psi}{\partial\theta}=Mu,\quad -\frac{\partial\psi}{\partial r}=Mv. \tag{2}$$

The relation between ψ and the axial vorticity ξ_s is

$$-\xi_s=\frac{1}{r}\frac{\partial}{\partial r}\left(\frac{r}{M}\frac{\partial\psi}{\partial r}\right)+\frac{1}{r}\frac{\partial}{\partial\theta}\left(\frac{1}{Mr}\frac{\partial\psi}{\partial\theta}\right). \tag{3}$$

In this paper, the contours of ψ are used to examine the secondary flow structure, and the maximum of stream func-

tion $\psi_{\max}$ that physically represents the volumetric flux of the secondary flow is used to measure the intensity of the secondary flow.

If the radius of the pipe is much smaller than that of curvature, that is $\kappa \ll 1$ and $M \approx 1$, the governing equations can be simplified. Similarly to Dean [17] for the stationary curved pipe flow, we drop the higher-order terms of κ and obtain the simplified governing equations

$$\frac{\partial ru}{\partial r} + \frac{\partial v}{\partial \theta} = 0, \tag{4a}$$

$$u\frac{\partial u}{\partial r} + \frac{v}{r}\frac{\partial u}{\partial \theta} - \frac{v^2}{r} = -\frac{\partial p}{\partial r} - \mathrm{De}^2 w\cos\theta(w+2F) - \frac{1}{r}\frac{\partial \xi_s}{\partial \theta}, \tag{4b}$$

$$u\frac{\partial v}{\partial r} + \frac{v}{r}\frac{\partial v}{\partial \theta} + \frac{uv}{r} = -\frac{1}{r}\frac{\partial p}{\partial \theta} + \mathrm{De}^2 w\sin\theta(w+2F) + \frac{\partial \xi_s}{\partial r}, \tag{4c}$$

$$u\frac{\partial w}{\partial r} + \frac{v}{r}\frac{\partial w}{\partial \theta} = G + \frac{2}{\mathrm{Ro}}(u\cos\theta - v\sin\theta) + \nabla^2 w, \tag{4d}$$

where $\nabla^2 = \partial^2/\partial r^2 + 1/r\ \partial/\partial r + 1/r^2\ \partial^2/\partial\theta^2$.

From these equations, the flow is dominated by De, F, and Ro. For the stationary case ($F=0$,Ro$\to\infty$), the flow is affected by only one parameter, the Dean number, which has been pointed out by Dean [17].

III. PERTURBATION SOLUTION

The simplified equations in the small curvature limit [Eqs. (4a)–(4d)] can be solved using the perturbation method when Ro$\to\infty$. We rewrite the simplified equations in the following form:

$$\left(-\frac{\partial\psi}{\partial\theta}\frac{\partial}{\partial\tilde{r}} + \frac{\partial\psi}{\partial\tilde{r}}\frac{\partial}{\partial\theta}\right)\nabla^2\psi = 2K(w+F)\tilde{r}\sin\theta\frac{\partial w}{\partial\tilde{r}} + 2K(w+F)\cos\theta\frac{\partial w}{\partial\theta} - \tilde{r}\nabla^4\psi, \tag{5a}$$

$$\frac{1}{\tilde{r}}\frac{\partial\psi}{\partial\theta}\frac{\partial w}{\partial\tilde{r}} - \frac{1}{\tilde{r}}\frac{\partial\psi}{\partial\tilde{r}}\frac{\partial w}{\partial\theta} = \tilde{G} + \nabla^2 w, \tag{5b}$$

where $\tilde{r}=2r$, $\tilde{G}=G/4$, $K=\mathrm{De}^2/8$. The boundary conditions are

$$\text{At } \tilde{r}=1.0, \quad \psi=0, \quad w=0. \tag{6}$$

For the small Dean numbers, ψ and w can be expanded in powers of K as

$$w = w_0(\tilde{r},\theta) + Kw_1(\tilde{r},\theta) + K^2 w_2(\tilde{r},\theta) + \cdots,$$
$$\psi = \psi_0(\tilde{r},\theta) + Kw_1(\tilde{r},\theta) + K^2\psi_2(\tilde{r},\theta) + \cdots. \tag{7}$$

The leading terms for w and ψ are the Poiseuille flow solutions,

$$w_0 = \frac{\tilde{G}}{4}(1-\tilde{r}^2), \quad \psi_0 = 0. \tag{8}$$

If the axial reference velocity w_m^* is the maximal axial velocity of the flow in a stationary straight pipe, then $\tilde{G}=4$.

Equating the coefficients of K terms, we obtain the first-order perturbation equations

$$\nabla^4\psi_1 = 2(w_0+F)\sin\theta\frac{\partial w_0}{\partial\tilde{r}}, \tag{9a}$$

$$\nabla^2 w_1 = \frac{1}{\tilde{r}}\frac{\partial\psi_1}{\partial\theta}\frac{\partial w_0}{\partial\tilde{r}} - \frac{1}{\tilde{r}}\frac{\partial\psi_1}{\partial\tilde{r}}\frac{\partial w_0}{\partial\theta}. \tag{9b}$$

Considering the boundary conditions, we obtain the solutions as

$$\psi_1 = \frac{\tilde{G}^2\sin\theta}{4608}\tilde{r}(1-\tilde{r}^2)^2(\tilde{r}^2-4) - \frac{F\tilde{G}\sin\theta}{192}\tilde{r}(1-\tilde{r}^2)^2, \tag{10a}$$

$$w_1 = \frac{\tilde{G}^3\tilde{r}(1-\tilde{r}^2)}{737280}(-19+21\tilde{r}^2-9\tilde{r}^4+\tilde{r}^6)\cos\theta + \frac{F\tilde{G}^2\tilde{r}(1-\tilde{r}^2)}{737280}(-120+120\tilde{r}^2-40\tilde{r}^4)\cos\theta. \tag{10b}$$

For the second order in K, we obtain

$$\tilde{r}\nabla^4\psi_2 = -\left(-\frac{\partial\psi_1}{\partial\theta}\frac{\partial}{\partial\tilde{r}} + \frac{\partial\psi_1}{\partial\tilde{r}}\frac{\partial}{\partial\theta}\right)\nabla^2\psi_1 + 2(w_0+F)\tilde{r}\sin\theta\frac{\partial w_1}{\partial\tilde{r}} + 2w_1\tilde{r}\sin\theta\frac{\partial w_0}{\partial\tilde{r}} + 2(w_0+F)\cos\theta\frac{\partial w_1}{\partial\theta}, \tag{11a}$$

$$\nabla^2 w_2 = \frac{1}{\tilde{r}}\frac{\partial\psi_2}{\partial\theta}\frac{\partial w_0}{\partial\tilde{r}} + \frac{1}{\tilde{r}}\frac{\partial\psi_1}{\partial\theta}\frac{\partial w_1}{\partial\tilde{r}} - \frac{1}{\tilde{r}}\frac{\partial\psi_1}{\partial\tilde{r}}\frac{\partial w_1}{\partial\theta}. \tag{11b}$$

The second-order solution is

$$\psi_2 = \frac{\tilde{G}^4\sin 2\theta}{118\,908\,518\,400}\tilde{r}^2(-1+\tilde{r}^2)^2(4979-2792\tilde{r}^2+777\tilde{r}^4 - 134\tilde{r}^6+5\tilde{r}^8) + \frac{FG^2\sin 2\theta}{118\,908\,518\,400}\tilde{r}^2(-1+\tilde{r}^2)^2 \times(49\,776\tilde{G}+114\,240F-19\,648\tilde{G}\tilde{r}^2-13\,400F\tilde{r}^2 - 6720F\tilde{r}^4+3328\tilde{G}\tilde{r}^4-576\tilde{G}\tilde{r}^6), \tag{12a}$$

$$w_1 = g_1(\tilde{G},F,\tilde{r}) + g_2(\tilde{G},F,\tilde{r})\cos(2\theta), \qquad (12b)$$

where $g_1(\tilde{G},F,\tilde{r})$ and $g_2(\tilde{G},F,\tilde{r})$ are complex expressions, both of them are only polynomial functions of $\tilde{r}$ with coefficients as functions of $\tilde{G}$ and F. This process of solving the higher-order terms presents no difficulty and can continue with the aid of a symbolic manipulation program on computers, except that it becomes increasingly laborious.

IV. NUMERICAL PROCEDURE

The full equations [Eqs. 1(a)–1(d)] and the simplified governing equations [Eqs. 4(a)–4(b)] are solved numerically. We first rewrite the equations in the following form:

$$\frac{\partial r J_r}{\partial r} + \frac{\partial J_\theta}{\partial \theta} = rJ. \qquad (13)$$

For the full equations,

$$J_r = u\phi - \frac{\partial \phi}{\partial r} + \frac{\kappa \cos\theta}{M}\phi, \quad J_\theta = v\phi - \frac{1}{r}\frac{\partial \phi}{\partial \theta} - \frac{\kappa \sin\theta}{M}\phi,$$

when $\phi = \xi_s$,

$$J = \frac{1}{r}\left\{ 2De^2 \cos\theta \left(\frac{w}{M} + F\right)\frac{\partial w}{\partial \theta} + 2De^2 r \sin\theta \left(\frac{w}{M} + F\right)\frac{\partial w}{\partial r}\right\},$$

when $\phi = w$,

$$J = \frac{G}{M} + \frac{2\kappa \cos\theta}{M} uw - \frac{2\kappa \sin\theta}{M} vw + \frac{2}{\mathrm{Ro}}(u\cos\theta - v\sin\theta).$$

For the simplified equations,

$$J_r = u\phi - \frac{\partial \phi}{\partial r}, \quad J_\theta = v\phi - \frac{1}{r}\frac{\partial \phi}{\partial \theta},$$

when $\phi = \xi_s$,

$$J = \frac{1}{r}\left\{ 2De^2 \cos\theta (w+F)\frac{\partial w}{\partial \theta} + 2De^2 r \sin\theta (w+F)\frac{\partial w}{\partial r}\right\},$$

when $\phi = w$,

$$J = G + \frac{2}{\mathrm{Ro}}(u\cos\theta - v\sin\theta).$$

The boundary conditions are

$$u = v = w = 0, \quad \psi = 0, \quad \xi_s = \frac{\partial v}{\partial r} \text{ at } r = 0.5. \qquad (14)$$

Equation (13) with Eqs. (2) and (3) and the boundary conditions, Eq. (14), are solved numerically by a finite volume method. The hybrid difference scheme is used for the convective and viscous terms (J_r and J_θ) and the central difference method is used for the source terms (J). After this, the governing differential equations become a set of algebraic equations. By adding the terms in the θ direction (J_θ) to the J terms, a trigonal matrix in the r direction, which can be solved by the triple diagonal matrix algorithm (TDMA) method, is obtained. A sweep is made in the θ direction. The equation of ψ [Eq. (2)] is solved by center difference scheme and the TDMA is also employed. For a given De number, an iterative procedure is applied to obtain the specific value of the axial pressure gradient G. First, we guess an initial value of G and compare the obtained mean axial velocity with the given value, that is, 1. If the former is smaller (or larger) than the latter, we increase (or decrease) G until their difference is smaller than 10^{-6}.

A uniform grid mesh system is employed in the whole cross section because boundary layers exist not only near the wall but also at the dividing boundaries of the secondary flow cells. The number of grids used is 21 in the r direction and 41 in the θ direction. The grid independence of the grid system is confirmed by repeating calculations with finer and coarser grids. The convergence criterion $|(\phi^{n+1} - \phi^n)/\phi^n| < 10^{-6}$, where n is the computational step number.

V. RESULTS AND DISCUSSIONS

A. Comparisons between the numerical results and the perturbation results

In the previous sections, we obtained both the numerical and perturbation solutions on the flow in rotating curved pipes with circular cross sections. Comparisons should be made between these solutions in order to find out the valid ranges of the simplified governing equations and the perturbation solution. Some results are shown in Figs. 2 and 3, and Tables 1 and 2.

Figure 2 shows the flow structure obtained from the three solutions for $\kappa = 0.02$. The numerical results based on the full equations are shown in the lower half cross section and those based on the simplified equations are shown in the upper half domain, the symbols in the upper half cross section represent the results from the perturbation solution. For De $= 10$, the three results are in good agreements. For De $= 20$, the results are still in good agreements for $F = -2.0$, $F = -1.0$, and $F = 0.0$. But for $F = 1.0$, the perturbation results are significantly different from the numerical results, indicating that the perturbation solution becomes invalid. Therefore, the valid range of the Dean number for the perturbation solution depends on the value of F. It is well known that the valid range of the perturbation solution for the stationary curved pipe flow is about De < 24. For rotating pipe, when the Rossby number is large, increasing F from zero to a positive value has the same effect as that of increasing the Dean number [7], so increasing F will decrease the valid range for the Dean number.

To find out the accuracy of the simplified governing equations, numerical calculations were carried out for De $= 150$ and the curvature from 0.001 to 0.2. Some results are shown in Fig. 3 for $\kappa = 0.02$ and $\kappa = 0.1$. The results from the simplified equations are plotted in the upper half domain, while the results from the full equations are shown in the lower half. For $\kappa = 0.02$ the two numerical solutions predict the

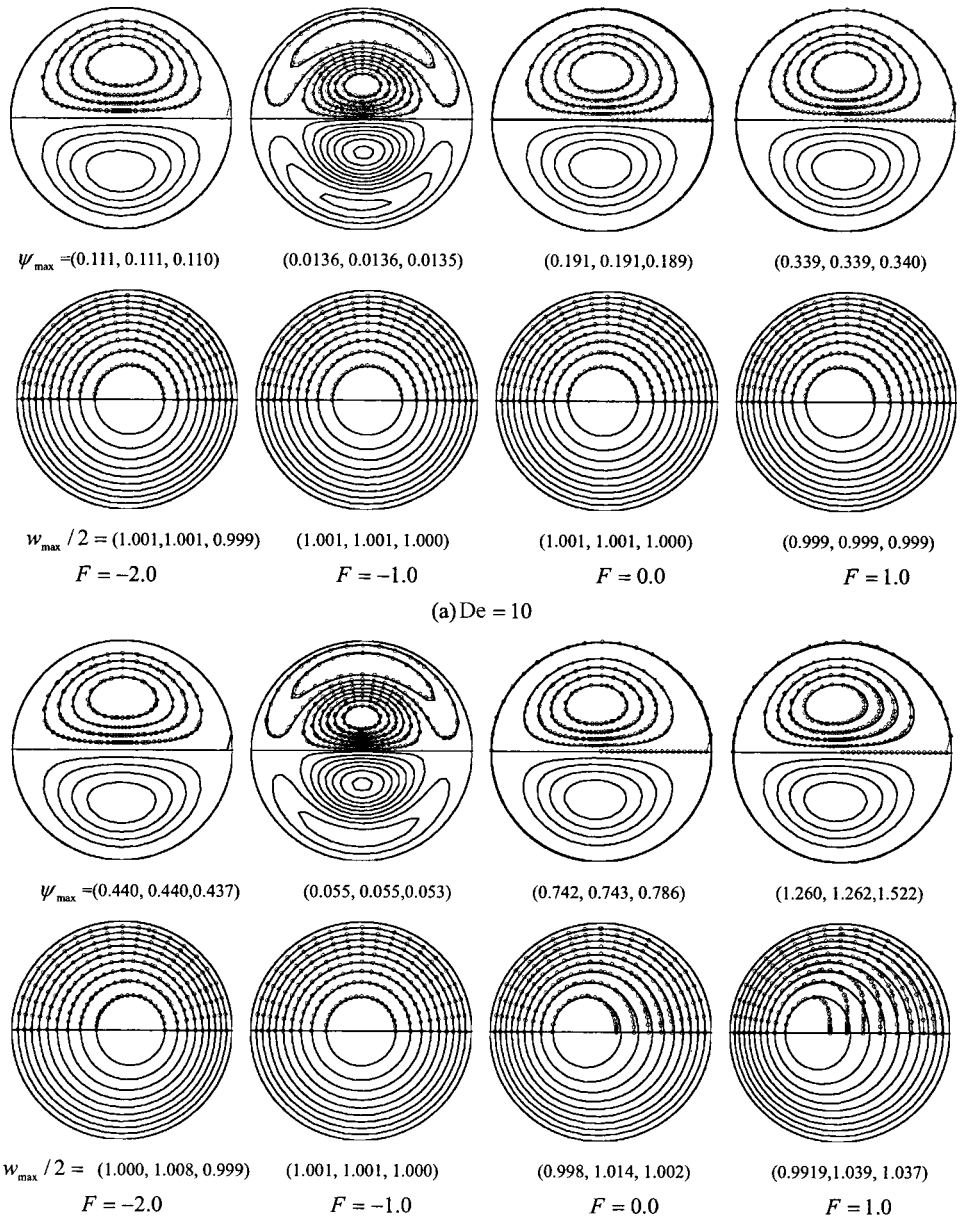

FIG. 2. Comparisons between numerical solutions and the perturbation solution for $\kappa=0.02$. Plots in the upper half cross section: numerical results based on the simplified equations. Plots in lower half cross section: numerical results based on the full equations. Symbols in the upper half cross section: results based on the perturbation solution $\psi_{\max}=(\psi^f_{\max},\psi^s_{\max},\psi^p_{\max})$, $w_{\max}/2=(w^f_{\max}/2,w^s_{\max}/2,w^p_{\max})$. Superscript f denotes numerical results from the full equation, superscript s denotes results from the simplified equation, superscript p denotes perturbation solution results.

same secondary flow structure and the distribution of the axial flow velocity. The maximal difference between the $\psi_{\max}$ is 0.3% for $-2\leqslant F\leqslant 1$. But for $\kappa=0.1$, the difference between the two numerical results becomes significant. As the curvature increases, the simplifications are no longer appropriate and the terms dropped through simplification become non-negligible.

The friction factor λ_c is another important flow property. It is obtained through balancing the forces along the axial direction:

$$\lambda_c\frac{1}{2}\rho w_m^{*2}2\pi R_c=-\frac{\partial p^*}{\partial s^*}\pi R_c^2. \tag{15}$$

Rewriting the above equation into dimensionless form, we obtain

$$\lambda_c\,\mathrm{Re}=-\frac{1}{2\,\mathrm{Re}}\frac{\partial p}{\partial s}. \tag{16}$$

Some results of the friction factor ratio λ_c/λ_s (λ_s is the friction factor of the flow in a stationary straight pipe) obtained from the three solutions are given in Tables I and II. Table I shows that when De$=10$ and $\kappa=0.02$, the three solutions almost all obtain the similar value with the maximum difference 0.13% in the range $-2\leqslant F\leqslant 1$. For De$=20$, the results are also in good agreements except for $F\geqslant 0.2$ (for $F=0.2$, the difference is 2.5%). The difference becomes larger as F increases further.

Tables I and II also show, for $F<-1.0$, the simplifications predict a greater friction factor ratio than the full governing equations, while for $F>-1.0$, they predict a smaller value. Some special discussions are needed for this phenom-

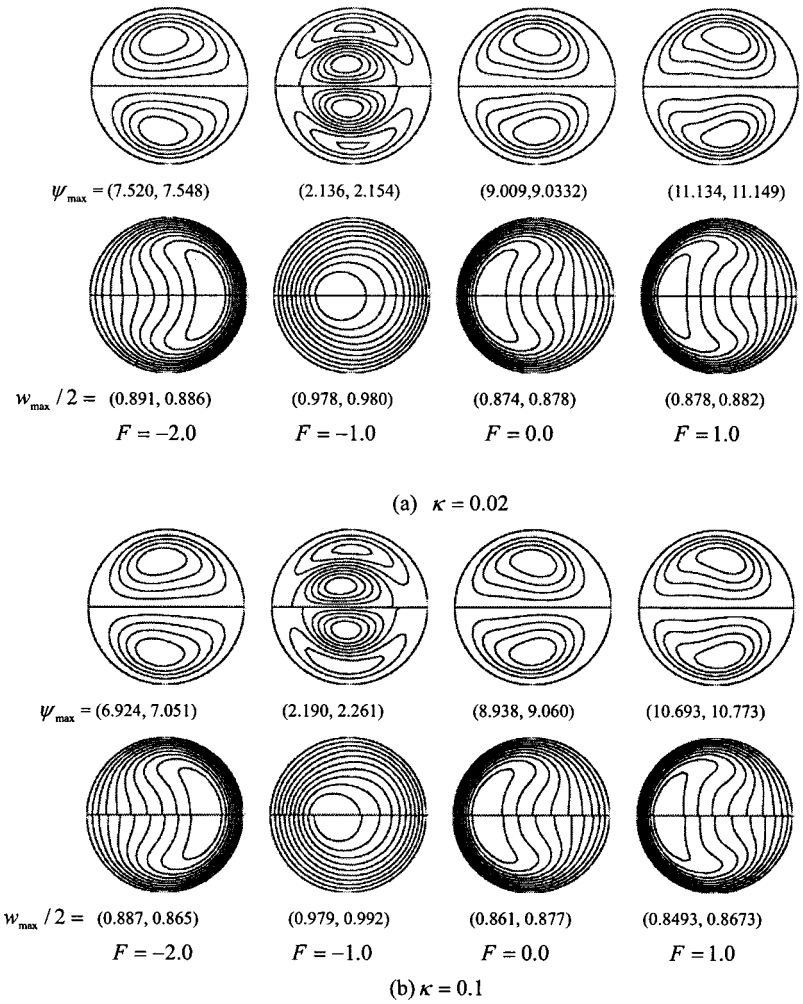

FIG. 3. Numerical result comparisons for De $=150$. Plots in the upper half cross section: numerical results based on the simplified equations. Plots in lower half cross section: numerical results based on the full equations $w_{\max}=(\psi^f_{\max},\psi^s_{\max}), w_{\max}/2=(w^f_{\max}/2, w^s_{\max}/2)$.

TABLE I. Comparisons of the friction factor ratio between the numerical results and perturbation results. Full: numerical results from the full governing equations. Simplified: numerical results from simplified governing equations. Perturbation: perturbation solution results.

	De$=10$ $\kappa=0.02$			De$=20$ $\kappa=0.02$		
F	Full	Simplified	Perturbation	Full	Simplified	Perturbation
−2	1.0017	1.0020	1.0011	1.0072	1.0081	1.0142
−1.8	1.0015	1.0017	1.0006	1.0045	1.0052	1.0081
−1.6	1.0014	1.0015	1.0003	1.0026	1.0031	1.0037
−1.4	1.0013	1.0014	1.0001	1.0016	1.0018	1.0010
−1.2	1.0013	1.0013	1.0000	1.0013	1.0013	1.0000
−1	1.0013	1.0012	1.0000	1.0019	1.0016	1.0007
−0.8	1.0014	1.0013	1.0002	1.0033	1.0014	1.0032
−0.6	1.0016	1.0013	1.0004	1.0055	1.0048	1.0074
−0.4	1.0018	1.0017	1.0008	1.0083	1.0074	1.0135
−0.2	1.0022	1.0017	1.0013	1.0117	1.0107	1.0217
0	1.0025	1.0022	1.0019	1.0157	1.0146	1.0322
0.2	1.0030	1.0026	1.0026	1.0202	1.0189	1.0452
0.4	1.0035	1.003	1.0034	1.025	1.0236	1.0612
0.6	1.004	1.0036	1.0044	1.0302	1.0287	1.0807
0.8	1.0046	1.0041	1.0054	1.0356	1.0339	1.1044
1	1.0053	1.0047	1.0066	1.0413	1.0393	1.1335

TABLE II. Comparisons of the friction factor ratio between the two numerical results for De=150.

	$\kappa=0.02$		$\kappa=0.1$		$\kappa=0.2$	
F	Full	Simplified	Full	Simplified	Full	Simplified
−2	1.5084	1.5155	1.5218	1.5558	1.5372	1.6025
−1.8	1.4492	1.4563	1.4563	1.4906	1.4642	1.5308
−1.6	1.3740	1.3812	1.3745	1.4104	1.3741	1.4447
−1.4	1.2500	1.2584	1.2410	1.2839	1.2266	1.3149
−1.2	1.0247	1.0278	1.0266	1.0431	1.0312	1.0666
−1	1.1954	1.1985	1.1979	1.2155	1.2001	1.2394
−0.8	1.2949	1.2936	1.3034	1.2980	1.3136	1.3057
−0.6	1.3686	1.3656	1.3788	1.3641	1.3909	1.3631
−0.4	1.4313	1.4274	1.4437	1.4246	1.4584	1.4214
−0.2	1.4863	1.4818	1.5019	1.4801	1.5203	1.4779
0	1.5357	1.5307	1.5553	1.5314	1.5782	1.5323
0.2	1.5808	1.5755	1.605	1.5795	1.633	1.5845
0.4	1.6224	1.6168	1.6516	1.6249	1.6851	1.6348
0.6	1.6612	1.6556	1.6959	1.6679	1.7349	1.6831
0.8	1.6978	1.6917	1.7375	1.7088	1.7824	1.7296
1	1.7319	1.7255	1.7774	1.7479	1.8280	1.7744

enon here. As examples, we take $F=1.0$ and $F=-2.0$. To get the simplified equations, we drop two terms in the source term J in Eq. (13) for the axial velocity equations that are

$$f_d=\frac{2\kappa\cos\theta}{M}uw-\frac{2\kappa\sin\theta}{M}vw=\frac{2\kappa u_s w}{1-\kappa x},$$

where u_s is the secondary flow velocity along the x coordinate (Fig. 1). When $F=1.0$, at the horizontal symmetry plane, $u_s<0$ which induces a negative f_d, so dropping the terms increases the axial flow rate and results in a smaller friction factor ratio. For $F=-2.0$, $u_s>0$ which induces a positive f_d, so dropping f_d results in a greater friction factor ratio.

B. Flow transitions with changing curvature

Most of the existing studies on curved rotating pipe are performed in the small curvature limit, based on the simplified governing equations, such as that of Daskopoulos and Lenhoff [12] and Ishigaki [7]. In engineering applications where large curvatures are often encountered, it is important and interesting to study the effects of curvature on the flow. In the present study where the full governing equations are solved numerically, it is easy to investigate the flow transitions with varying curvature while keeping the other parameters constant.

Ishigaki [7] studied the flow variations with F in detail. Here we chose $F=-1.3$ and De=250 to study the effects of the curvature. The secondary flow streamlines and the contours of the axial flow velocity are shown in Fig. 4. The outer bend is on the left. The dotted lines represent the coclockwise secondary vortices.

As shown in Fig. 4, when $\kappa=0.001$, the secondary flow has a four-cell structure, the larger vortices near the wall are due to the Coriolis force, while the smaller ones are due to the centrifugal force. This phenomenon has been reported by Ishigaki [7] for F around -1. As the curvature increases, the secondary flow cells due to the centrifugal force are intensified, their sizes become larger and larger, until at last they take up the right half cross section. The maximum of the stream function $\psi_{\max}$ which represents the intensity of the net secondary flow, first decreases and then increases as the curvature increases.

The source terms of the axial vorticity ξ_s are

$$rJ=2\,\mathrm{De}^2\cos\theta\left(\frac{w}{M}+F\right)\frac{\partial w}{\partial\theta}+2\,\mathrm{De}^2 r\sin\theta\left(\frac{w}{M}+F\right)\frac{\partial w}{\partial r}.$$

For small curvatures, $M\approx1$, and increasing the curvature does not modify the source term significantly. But for a relatively large curvature, increasing the curvature increases w/M with an increasingly large centrifugal force. In the

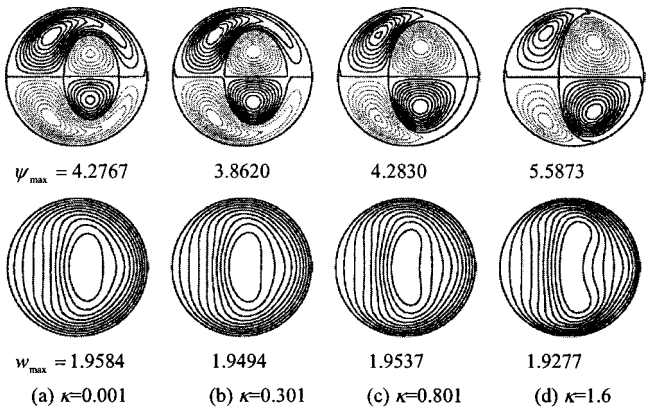

FIG. 4. Flow variations with curvature for De=250 and $F=-1.3$. Out bend is on the left. Upper plots, contours of stream function. Lower plots, contours of axial flow velocity.

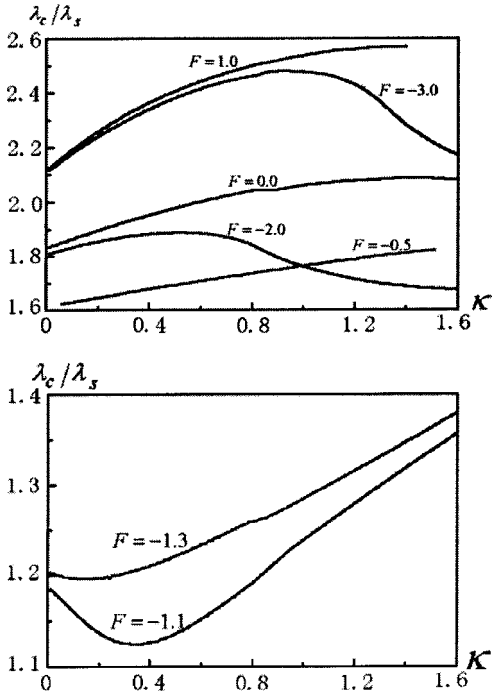

FIG. 5. Curves of the friction factor as a function of curvature for De=250.

present case, F and De are kept constant, the increase in κ will intensify the secondary flow due to the centrifugal force.

For the axial flow velocity, Fig. 4 indicates that the location of the maximum axial velocity is divided into two locations as the curvature increases. The contours are distorted and seem to be pulled to the inner bend and outer bends at the same time.

The effects of the curvature on the friction factor ratio are shown in Fig. 5 for different F. When F is around -1, e.g., $F=-1.1$ and -1.3, the friction factor ratio first decreases and then increases with increasing curvature. For $F=1.0$ and 0.0, the friction factor ratio increases with curvature, while for $F=-2.0$ and -3.0, the friction factor ratio first increases and then decreases with curvature. All these phenomena have never been reported in literatures and we hope to verify them in future experiments. When we take into account the variations of the secondary flow intensity, these phenomena may be explained. Because the friction factor determines the flow pressure drop along the axial direction, these variations may be of significance in engineering applications.

C. Flow transitions with changing Rossby number

For a small Rossby number, the flow will appear as a Taylor-Proudman phenomenon. This flow structure has been reported by Ishigaki [7] based on the simplified equations, in which the Rossby number is an independent parameter. Based on the full governing Eqs. (1a)–(1d), it is easily found that the Rossby number is not an independent parameter and can be written as $\mathrm{Ro}=1/(F\kappa)$. To approach a small Rossby number, two procedures may be employed: (i) keeping F constant, while increasing curvature κ; (ii) keeping κ constant, while increasing F. In fact, Ishigaki [7] studied the

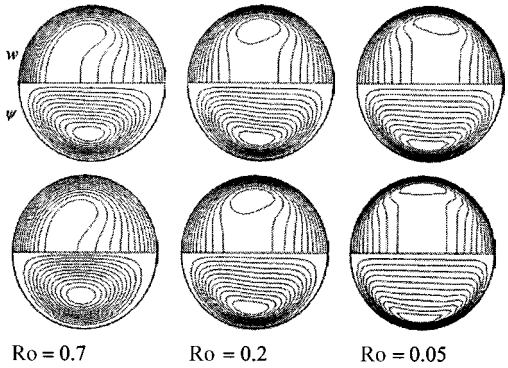

FIG. 6. Flow variations with Ro for De=20. The out bend is on the left. Upper, results from procedure (i) for $F=50$; lower, results from procedure (ii) for $\kappa=0.1$.

flow structure with varying Ro only along procedure (i). In this study, we will examine the variations of flow natures with Ro along the two procedures to find the lost information due to the simplifications of the governing equations.

Figure 6 shows the flow structure with varying Ro. This figure indicates that both procedures can produce the similar Taylor-Proudman phenomenon. When Ro is small such as 0.05, the flow structure is almost symmetrical about the y axis and the axial velocity is nearly constant in the core region and contours are shaped like a dumbbell. This can be explained qualitatively as the following: considering the terms in w equation (Eq. 4d) relative to the Rossby number are

$$\frac{2}{\mathrm{Ro}}(u\cos\theta - v\sin\theta)=\frac{2}{\mathrm{Ro}}u_s .$$

For a positive Ro, near the horizontal symmetrical plane, $u_s<0$ and the above expression is negative and reduces the local axial velocity, while near the upper and lower wall, $u_s>0$ which increases the axial velocity near the wall. When Ro is large, this effect is negligible because the above expression is very small. But when Ro becomes smaller, the above expression becomes larger, until at last it results in a dumbbell-like shape of the axial velocity contours with two high velocity regions near the upper and lower walls.

Although the two procedures produce very similar flow structures, they predict very different secondary flow intensities and the frication factor ratios. Figure 7 shows the curves of the maximum of the stream function and the friction factor ratio as functions of the Rossby number obtained from the two procedures. When the Rossby number decreases, for procedure (i), the secondary flow intensity increases with the increasing Rossby number, while for procedure (ii), the secondary flow intensity first increases then decreases. Although the friction factor ratios obtained from the two procedures both decrease as the Rossby number increases, the values are very different for the same Rossby numbers. Because Ro is an independent parameter for the simplified equations, when De and F are specified, there is

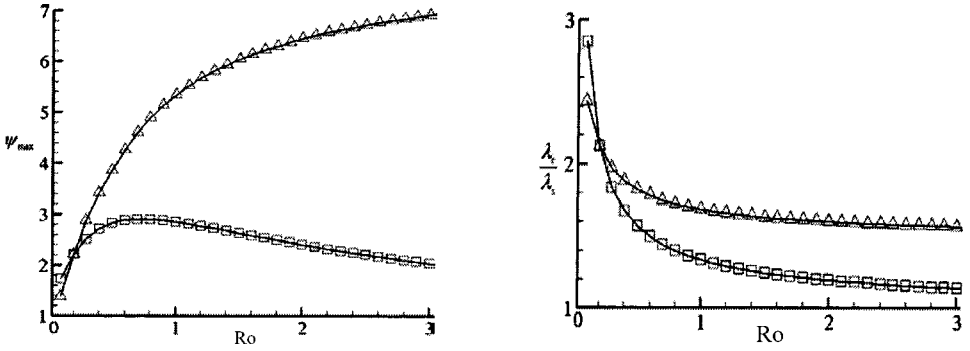

FIG. 7. Variations of the stream function maximum and the friction factor ratio with Ro. Delta, results from procedure (i); square, results from procedure (ii). Parameters' values are the same as in Fig. 6.

only one curve of ψ_{max} with the varying Ro. Ishigaki [7] made concluded that the secondary flow wakens as |Ro| decreases. According to the present study, this conclusion is not exact because it only follows procedure (i), while procedure (ii) is omitted because of the small curvature simplification.

D. Flow structure for the high Dean numbers

In the previous sections, the effects of curvature and valid range of the simplified equations are analyzed, which are the main purposes of the present study. In this section, we will discuss the flow structure for the high Dean numbers. When the Dean number exceeds a critical value, the flow equations have multiple solutions. Daskopoulos and Lenhoff [12] studied the flow bifurcation, but the imposed symmetry in their simulation caused loss of some flow branches. Like Daskopoulos and Lenhoff, Ishigaki [7] obtained the secondary flow cells due to the flow instabilities, but only one flow branch was predicted. In order to find out the multiple solutions for the high Dean numbers, the present study employs two numerical procedures: one procedure has symmetry imposed to find the symmetric stable flow branch like Ishigaki [7]; the other has no symmetry imposed to detect the unconditionally stable flow branches.

The results for De=450, $\kappa=0.1$ obtained through the two numerical procedures are shown in Fig. 8. For $F=-0.9$, the two procedures both produce the unconditionally stable solution, the distributions of the axial velocity and the secondary flow are similar to those for the small Dean numbers. For $F=-1.02$, the no-symmetry-imposed procedure still produces the unconditional stable solution, while the symmetry imposed procedure produces a completely different flow structure—the symmetric stable solution. The streamlines show three vortices in the lower half cross section: two due to the centrifugal force and the Coriolis force, one due to the flow instability (the Dean vortex, the vortex near the symmetry plane). The location of the axial flow velocity is divided into two locations that appear in the boundaries between the Dean vortex and the vortex due to the centrifugal force. The potential sources of the instability for flows in a rotating curved pipe are the centrifugal force and the Coriolis force. The centrifugal force produces a secondary flow that moves towards outer bend along the horizontal symmetry plane and tends to give rise of flow instability, the secondary flow due to the Coriolis force pointing inwards acts as the disturbance at $\theta=\pi$ near the outer wall for counter-rotation, then the bifurcation emerges and the Dean vortex is generated if the Dean number exceeds a critical value. As F decreases, for the unconditionally stable solution, the secondary vortices due to the centrifugal force becomes small, while for the symmetrical solution, the secondary flow due to the Coriolis force and the Dean vortex combine each other because of the same rotating direction, the secondary flow due to the centrifugal force becomes weak and completely disappears at $F=-1.20$. At this value, the axial velocity still has two maximum regions. At $F=-1.40$, because the increase of Coriolis force reduces the effect of centrifugal force, the flow instability disappears and the two numerical procedures give the same unconditionally stable solution.

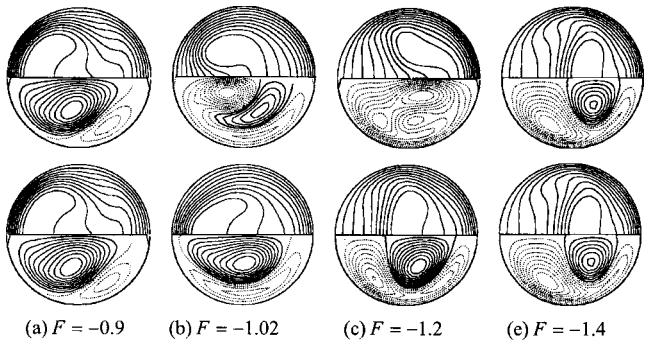

FIG. 8. Flow structures for De=450, $\kappa=0.1$. Upper plots, solution with imposed symmetry; lower plots, solution without imposed symmetry.

VI. CONCLUSIONS

Most of the previous valuable studies on the flow in rotating curved pipes with circular cross sections were based on the simplified equations for small curvatures and no author focused on the effects of the curvature. In the present study, we numerically solved the full governing equations and numerically and analytically solved the simplified governing equations. Based on the calculations, we elucidated the lost information because of the simplification. Based on the numerical results from the full governing equations, we discussed the effects of curvature on the flow structure and friction factor ratio for the high and low Rossby numbers. We also detected two flow branches from

the full governing equations through two numerical procedures. One issue that remains is the effects of the curvature on the bifurcation diagram and the critical parameters. This will be studied in future work.

ACKNOWLEDGMENT

This research is supported by the U.S. Department of Energy under Contact No. W-7405-ENG-36.

[1] H. Ludwieg, Ingenieurs **19**, 296 (1951).
[2] H. Miyazaki, Int. J. Heat Mass Transf. **14**, 1295 (1971).
[3] H. Miyazaki, Trans. ASME, Ser. C: J. Heat Transfer **95**, 64 (1973).
[4] H. Ito and T. Motai, Rep. Inst. High Speed Mech. **29**, 33 (1974).
[5] M. M. Menon, M.S. thesis, Case Western Reserve University, 1984 (unpublished).
[6] H. Ito, H. Komaki, S. Hasegawa, and M. Suzuki, Mem. Inst. High Speed Mech. **58**, 185 (1987).
[7] H. Ishigaki, J. Fluid Mech. **329**, 373 (1996).
[8] L. Q. Wang and K. C. Cheng, Phys. Fluids **8**, 1553 (1996).
[9] K. Yamamoto, S. Yanase, and M. M. Alam, J. Phys. Soc. Jpn. **68**, 1173 (1999).
[10] J. Zhang, B. Zhang, and J. Ju, Int. J. Heat Fluid Flow **22**, 583 (2001).
[11] B. Zhang, Q. Chen, and J. Zhang, J. Hydrodynam. **13**, 75 (2001).
[12] P. Daskopoulos and A. M. Lenhoff, J. Fluid Mech. **217**, 575 (1990).
[13] M. Selmi, K. Nandakumar, and W. H. Finlay, J. Fluid Mech. **262**, 353 (1994).
[14] M. Selmi and K. Nandakumar, Phys. Fluids **11**, 2030 (1999).
[15] L. Wang and K. C. Cheng, Phys. Rev. E **51**, 1155 (1995).
[16] S. Liu and J. H. Masliyah, J. Fluid Mech. **251**, 315 (1993).
[17] W. R. Dean, Philos. Mag. **7**, 208 (1927).